Oxygen vacancy-attired dual-active-sites Cu/Cu$_{0.76}$Co$_{2.24}$O$_4$ drives electron transfer for efficient ammonia borane dehydrogenation

Chenyang Wang [a,b], Yangyang Ren [a], Jianling Zhao [a], Shuo Sun [a], Xihua Du [a], Mengmeng Wang [a], Gang Ma [a], Haoran Yu [a], Lanlan Li [a], Xiaofei Yu [a], Xinghua Zhang [a], Zunming Lu [a], Xiaojing Yang [a,*]

[a] *School of Materials Science and Engineering, Hebei University of Technology, Tianjin 300130, China*
[b] *Department of Applied Chemistry, Yuncheng University, Yuncheng 044000, China*

ABSTRACT

In the ammonia borane (AB) hydrolysis reaction, overcoming the weak activation of H$_2$O by metal catalysts can be achieved by introducing transition metal oxides (TMOs) for catalyst active-sites design. Herein, we uncovered that oxygen vacancy (V$_O$)-attired Cu/Cu$_{0.76}$Co$_{2.24}$O$_4$ dual-active-sites catalysts significantly increase the hydrogen production rate of AB hydrolysis. The turnover frequency of Cu/Cu$_{0.76}$Co$_{2.24}$O$_4$-V$_O$ dehydrogenation in 0.10 M NaOH can reach 50.33 mol$_{H2}$/(mol$_{cat}$·min), which is 45.9 times that of metal Cu. By means of a joint experimental and computational study, the V$_O$ defects promote the formation of electron-rich surface of Cu$_{0.76}$Co$_{2.24}$O$_4$, and the Cu also enriches the surface electrons due to the strong interaction with TMOs, which enhances the activation of O–H and B–H bonds, respectively, and significantly accelerates the rate-determining step of the reaction. This work demonstrates the important role of constructive defects in regulating surface electrons of dual-active-sites catalysts on the performance enhancement and provides a broader idea for the design of excellent AB hydrolysis catalysts.

1. Introduction

Hydrogen has the potential to become an alternative energy source to fossil fuels due to its environmental friendliness and sustainability characteristics [1,2]. Hydrogen can be obtained by a variety of technologies, the most promising of which is the decomposition of water and hydrogen storage materials [3–6]. Ammonia borane (NH$_3$BH$_3$, AB), as a hydrogen storage material, with a hydrogen storage content of 19.6 wt %, is non-toxicity, and high stability in both aqueous solutions and air at room temperature [7–9]. Hydrolysis of AB can release 3 equivalents of hydrogen in the presence of a catalyst. Metals are usually used as catalysts to show excellent catalytic activity [10–14].

In recent years, studies on the hydrolysis mechanism have shown that H$_2$O molecule activation is the rate-determining step (RDS) of AB hydrolysis [15,16]. However, in the metal-catalyzed hydrolysis reaction, the metal only has a good activation effect on AB molecules, but the adsorption energy is low and the activation energy barrier is high for H$_2$O molecules, therefore the catalytic activity of hydrolysis of AB is severely hampered [17–19]. Chen and co-workers reported that Pt/WO$_3$

catalysts showed TOF is 710.1 mol$_{H2}$ mol$_{Pt}^{-1}$ min^{-1} for AB hydrolysis [20]. Co-CoO$_x$@NCS-II prepared by Zhang et al. demonstrated a superior specific hydrogen generation rate of 5562 mL min^{-1} g$_{Co}^{-1}$ [21]. The activation and dissociation of H$_2$O molecules by TMOs has been proven in many aspects of studies [22,23]. Therefore, forming a heterogeneous structure between metal and TMOs is an effective strategy to improve the catalytic activity of hydrolysis. However, the current metal/TMOs heterostructure only studies the improvement of activity by the simple combination between the two, and the promotion mechanism is only speculated. The close synergy effects between the two active sites of the metal/TMOs structure has not been clearly explained.

Simultaneous optimization of the two active sites is particularly important when forming dual-active-sites catalysts. Although there are many methods for optimizing the catalytic activity of metal sites, in the study of metal-based catalysts, increasing the electron density on the metal surface is an effective method to enhance the metal's adsorption and attack on the reactants [24–26]. However, in metal/TMOs catalysts, TMOs provides electrons to the metal with a corresponding decrease in its own surface electron density, and the catalytic effect of this active site

may be reduced. Therefore, the simultaneous guarantee of the catalytic activity of the dual active sites requires some specific optimization methods. The lattice oxygen can be separated under certain conditions to form oxygen vacancies (V_O) [27]. The unique electron vacancies formed by V_O can be regarded as electron donors that can modulate certain surface electronic properties of TMOs, thus forming effective active sites for adsorption and catalysis and can adjust the surface electronic properties of the overall catalyst [28,29]. In light of the above considerations, under the coordination of rational construction and electronic structure regulation, it can be expected to design dual-active-sites catalysts for AB dehydrogenation. Among the low-cost non-noble metals, the synergistic effect of Cu and Co is more favorable to the AB hydrolysis reaction compared with other non-noble metals. In addition, the transient Cu–H generated by CuO reduction also has better catalytic effect and facilitates hydrogen generation, which is expected to play an active role in catalytic AB hydrolysis process [30,31].

Herein, a strategy was proposed to design and manufacture of metal/ TMOs heterostructure catalysts with optimized active-sites. Hollow nanospheres structures of $CuO/Cu_{0.76}Co_{2.24}O_4$ are synthesized by the self-templating method, followed by simple ascorbic acid (AA) to form V_O-attired $Cu/Cu_{0.76}Co_{2.24}O_4$ exhibits excellent AB hydrolysis performance. As expected, the metallic Cu and $Cu_{0.76}Co_{2.24}O_4$ in Cu/ $Cu_{0.76}Co_{2.24}O_4$-V_O can effectively activate AB and H_2O molecules, respectively, to facilitate the hydrolysis process. Benefiting from the effect of V_O defects on the surface electronic structure and electron transfer between active sites in the heterostructure, the developed dual-active-sites catalyst exhibits significantly better catalytic activity than the pure-phase structure. Furthermore, the mechanism of the synergy of defect-attired heterostructures on performance optimization stimulates a new consideration on the development of noble metal-free dual-active-sites catalytic systems.

2. Experimental section

2.1. Synthesis of catalysts

2.1.1. Preparation of $CuO/Cu_{0.76}Co_{2.24}O_4$ hollow nanospheres

$CuO/Cu_{0.76}Co_{2.24}O_4$ was synthesized by a previously reported hydrothermal method [32]. 0.42 mmol $Co(NO_3)_2·6H_2O$ and 0.21 mmol $Cu(NO_3)_2·xH_2O$ were added to 6 mL ethylene glycol and 31 mL isopropanol to form a homogeneous transparent solution. After stirring for 90 min, the solution was transferred into a Teflon-lined stainless-steel autoclave and maintained at 180 °C for 1 h. The precipitate was centrifuged, washed with ethanol, and then dried for 2 h to obtain $CuO/Cu_{0.76}Co_{2.24}O_4$ precursor. Precursors are calcined in a muffle furnace at 350 °C for 3 h with the heating rate is 2 °C/min. Finally, $CuO/Cu_{0.76}Co_{2.24}O_4$ hollow microspheres are obtained.

Besides, $CuO/Cu_{0.76}Co_{2.24}O_4$ with different CuO contents are obtained by changing the addition molar ratio of Co:Cu to 2:0.8, 2:2, and 2:3, respectively. For comparison, pure $Cu_{0.76}Co_{2.24}O_4$ were synthesized by the same strategy with the molar ratio of Co:Cu = 2:0.7; pure CuO is obtained by the molar ratio of Co:Cu of 0:1. And the sample after the activation period of the catalytic reaction is taken out after the $CuO/Cu_{0.76}Co_{2.24}O_4$ is subjected to the AB catalytic reaction at room temperature for 1 min, washed with deionized water, and freeze-dried.

2.1.2. Preparation of dual-active-sites $Cu/Cu_{0.76}Co_{2.24}O_4$ catalysts

The dual-active-sites $Cu/Cu_{0.76}Co_{2.24}O_4$ catalysts were obtained by soaking $CuO/Cu_{0.76}Co_{2.24}O_4$ in AA solution, which are V_O attired $Cu/ Cu_{0.76}Co_{2.24}O_4$ (denoted as $Cu/Cu_{0.76}Co_{2.24}O_4$-V_O). Soak 0.06 g $CuO/ Cu_{0.76}Co_{2.24}O_4$ in 20 mL AA solution (0.009 g/mL) for 60 min and then the solution was centrifuged and washed 5 times with deionized water to remove the participating impurities, after which the precipitate was freeze-dried to obtain a black powder as a V60 sample. Among them, the content of surface V_O is obtained by adjusting the reduction time. The reduction time is 0, 10, 30, and 90 as V0, V10, V30, and V90.

For comparison, the AA treated $Cu_{0.76}Co_{2.24}O_4$ (denoted as $Cu_{0.76}Co_{2.24}O_4$-V_O) were obtained by soaking $Cu_{0.76}Co_{2.24}O_4$ in AA solution. Similarly, AA reduction treats CuO for t min, denoted as CuO-Vt, where t is 60 and 120, respectively.

2.2. Characterization techniques

Powder X-ray diffraction (XRD) patterns were collected on Bruker (D8 Discover) with Cu Kα radiation and scan rates of 6 and 0.24°/min. The results of the 0.24°/min scanning rates are used for Rietveld analysis. Scanning electron microscopy (SEM) imaging and energy dispersive X-ray spectroscopy (EDS) were performed by Quanta 450 FEG. Transmission electron microscopy (TEM) images were taken on a Talos F200S apparatus. X-ray photoelectron spectra (XPS) were recorded using ESCALAB 250Xi with an Al-Kα X-ray source. The charging shift was calibrated using C 1s photoemission line at 284.8 eV in XPS data analysis. Raman spectra were collected on InVia Reflex with a 532 nm laser source. The specific surface area and pore volume of samples were calculated by N_2 adsorption−desorption at 77 K on ASAP 2460 using the Brunauer−Emmett−Teller and Barrett−Joyner−Halenda methods, respectively. The AutoChem II 2920 apparatus with a thermal conductivity detector (TCD) was used to perform temperature-programmed desorption of O_2 (O_2-TPD). The procedures were described as follows: (1) prior to each test, the samples were pretreated at 200 °C for 2 h in an inert gas stream (He) to clean the surface; (2) catalysts were cooled to 50 °C for 1 h under O_2 adsorption; (3) purging with He for 1 h to remove any surface physically adsorbed gases and residual feed gas from the streams; and (4) heating from 50 to 900°C at a rate of 10 °C/min.

2.3. Dehydrogenation of AB

The prepared samples were used as catalysts for the hydrolysis of AB at room temperature (25 °C) and the volume of H_2 gas generation was recorded using a bi-channel micro-gas flowmeter (RTK-TGMC). Typically, 8 mg of catalyst was dispersed in 9 mL of H_2O and sonicated for 10 min to obtain a uniformly dispersed solution. After that, 1 mL of 14 g/L of AB solution (0.45 mmol) was injected into the solution to start the hydrolysis reaction. The process of AB hydrolysis was described as follows:

$$NH_3BH_3 + 2H_2O \rightarrow NH_4BO_2 + 3H_2 \tag{1}$$
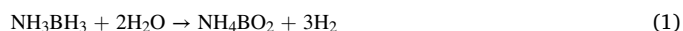
The catalytic activity of samples was evaluated by turnover frequency (TOF) value:

$$TOF = n_{H2} / (n_{cat} \times t) \tag{2}$$

in which n_{H2} is the mole number of generated H_2, n_{cat} is the mole number of catalysts, t is the reaction time in unit of minutes. Among them, the amount of $Cu/Cu_{0.76}Co_{2.24}O_4$-V_O calculated according to the refinement results is 0.0424 mmol. To assess the durability of the catalyst, only the reaction AB solution (10 mL, 1.4 g/L) was replaced after the completion of a reaction to perform 5 cycles of the experiment. The apparent activation energy (E_a) required for the reaction was investigated by varying the experimental temperature to 30, 35, and 40 °C. In order to investigate the kinetic isotope effect, the reaction was also conducted by replacing H_2O with D_2O as the reactant over different catalysts at the same reaction conditions.

2.4. Calculation details

The present first principle calculations were performed by the Vienna ab initio simulation package (VASP) using the generalized gradient approximation (GGA) and Perdew-Burke-Ernzerhof (PBE) method base on density functional theory (DFT). The projector augmented wave (PAW) was used to describe ions and electron interaction. The kinetic energy cutoffs was set at 300 eV. In the process of

simulating crystal surface calculation, to avoid repetition for surface interaction, the distance of vacuum spacing in discontinuous direction was 15 Å. In all the calculations, we use $3 \times 3 \times 1$ for the Monkhorst-Pack k-point for periodic crystal structure and surface model. The convergence threshold for energy was set at 10^{-5} eV. The equilibrium lattice constants were optimized with maximum stress on each atom within 0.05 eV/Å. The Hubbard U (DFT+U) corrections for 3d transition metal (Co) were set as 3.25 eV.

The adsorption energy (ΔE_{ads}) were defined as follows

$$\Delta E_{ads} = E_{ad}/E_{sub} - E_{ad} - E_{sub} \tag{3}$$

where E_{ad}/E_{sub}, E_{ad}, and E_{sub} are the total energies of the optimized adsorbate/substrate system, the adsorbate in the structure, and the clean substrate, respectively.

The free energy was calculated using the equation:

$$G = E + ZPE - TS \tag{4}$$

where G, E, ZPE, and TS represented the free energy, total energy from DFT calculations, zero-point energy, and entropic contributions (T was set to be 300 K), respectively.

3. Results and discussion

3.1. Characterization of structure of catalysts

The prepared $CuO/Cu_{0.76}Co_{2.24}O_4$ is confirmed as a composite of CuO and $Cu_{0.76}Co_{2.24}O_4$ by XRD. The crystal structure parameters and the content of each phase were refined by Rietveld analysis using the Rietan-2000 program (Fig. 1a). The calculated fitting curve of $CuO/Cu_{0.76}Co_{2.24}O_4$ (black line) has a good overlap with the original XRD data (red dots), and the error curve (blue line) fluctuates slightly. R-weighted pattern (Rwp) and goodness fit (S) that determine the reliability of the refined results are listed in Table 1. $CuO/Cu_{0.76}Co_{2.24}O_4$ is precisely determined to consist of 85.8 wt% $Cu_{0.76}Co_{2.24}O_4$ and 14.2 wt % CuO. The cell parameters of CuO change significantly from the initial standard values of a, c, and β angles, indicating significant lattice enlargement and distortion. It shows that the close contact between the two TMOs causes the unit cell parameters to change.

The phase structure characterization of $CuO/Cu_{0.76}Co_{2.24}O_4$ after being reduced by AA is shown in Fig. 1b and c. The diffraction peaks at $2\theta = 31.2, 36.8, 44.7, 59.3$, and $65.1°$ can correspond to the face-centered cube structure of $Cu_{0.76}Co_{2.24}O_4$ (220), (311), (400), (511), and (440) planes, and the peaks at $2\theta = 35.5°$ is indexed to characteristic (002) plane of CuO structure. Among them, the diffraction peak of the CuO structure gradually disappears with the increase of the reduction time, and the structures of V60 and V90 did not include CuO. At the same time, the $Cu_{0.76}Co_{2.24}O_4$ (311) crystal plane diffraction peaks of V60 and V90 shifted to the low angle direction which can be ascribed to the presence of structural defects [28]. Besides, there is a diffraction peak at $2\theta = 43.3°$ gradually appears with the reduction of AA, which is the Cu (111) plane. As a comparison, pure $Cu_{0.76}Co_{2.24}O_4$ only shows the diffraction peak of the (311) plane shift after the reduction process (Fig. S1a, b), while the (111) plane diffraction peak of pure CuO disappears and the Cu (111) diffraction peak shows (Fig. S1c). CuO is
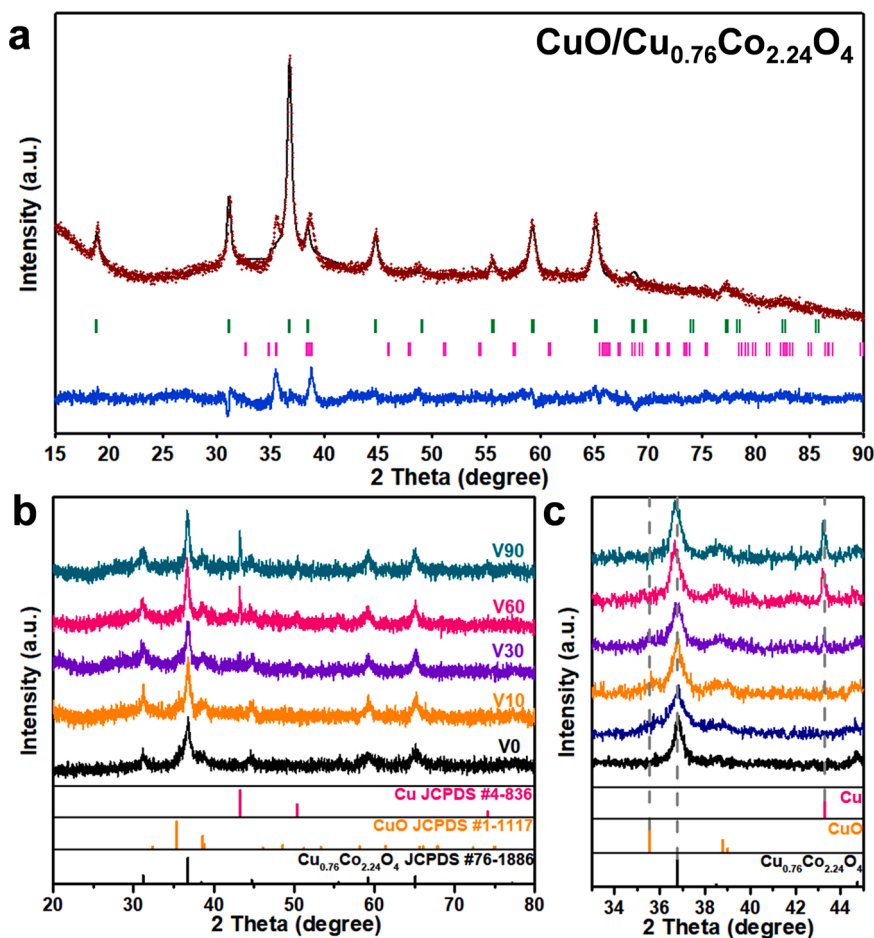

Fig. 1. Rietveld refined XRD patterns of $CuO/Cu_{0.76}Co_{2.24}O_4$ with experimental data (red dots), calculated profiles (black line), allowed Bragg diffraction positions (the green vertical bars belong to $Cu_{0.76}Co_{2.24}O_4$ and pink bars belong to CuO) and the difference between the calculated and observed intensities (blue line) (a). XRD patterns of $Cu/Cu_{0.76}Co_{2.24}O_4$-V_O with different reduction time (b) and analysis of partial enlargement (c).

Table 1

According to Rietveld refined $CuO/Cu_{0.76}Co_{2.24}O_4$ XRD data, the lattice parameters and phase content of $Cu_{0.76}Co_{2.24}O_4$ and CuO, and the reliability of the results.

Parameters	$Cu_{0.76}Co_{2.24}O_4$	CuO				Rwp (%)	S
	a (Å)	a (Å)	b (Å)	c (Å)	β (°)		
Standard	8.098	4.689	3.422	5.130	99.59	1.16	1.55
Calculated	8.104	4.801	3.425	5.277	100.04	(<10)	(<3)
Contents (wt%)	85.8	14.2					

completely reduced to metallic Cu in $CuO/Cu_{0.76}Co_{2.24}O_4$ when the AA reduction time exceeded 60 min, while pure CuO requires 120 min, which is due to the larger size of pure CuO with the same morphology and poor dispersion compared to heterostructures. Therefore, the above results indicate that Cu was successfully generated from CuO during the AA reduction of the heterostructure, while the $Cu_{0.76}Co_{2.24}O_4$ is maintained.

The SEM image of the pure $Cu_{0.76}Co_{2.24}O_4$ shows that the nanospheres exhibit a smoother surface, and the average diameter of the spheres is about 540 nm (Fig. S2a). For $CuO/Cu_{0.76}Co_{2.24}O_4$, the size of the nanospheres did not change significantly, but some obvious particle protrusions appeared on the surface (Fig. S2b). Further observation of $CuO/Cu_{0.76}Co_{2.24}O_4$ by TEM shows that nanospheres are assembled from numerous nanoparticles and exhibit a hollow structure which could enhance the full contact area between the reactant molecules and catalysts [33]. The average surface shell thickness of the hollow nanosphere about 140 nm and an inside hollow cavity diameter of about 220 nm (Fig. 2a, b). HRTEM was performed on hollow sphere edge particles as shown in Fig. 2d. The $CuO/Cu_{0.76}Co_{2.24}O_4$ exhibits the lattice fringes with interlayer distances of 0.28 and 0.24 nm, which
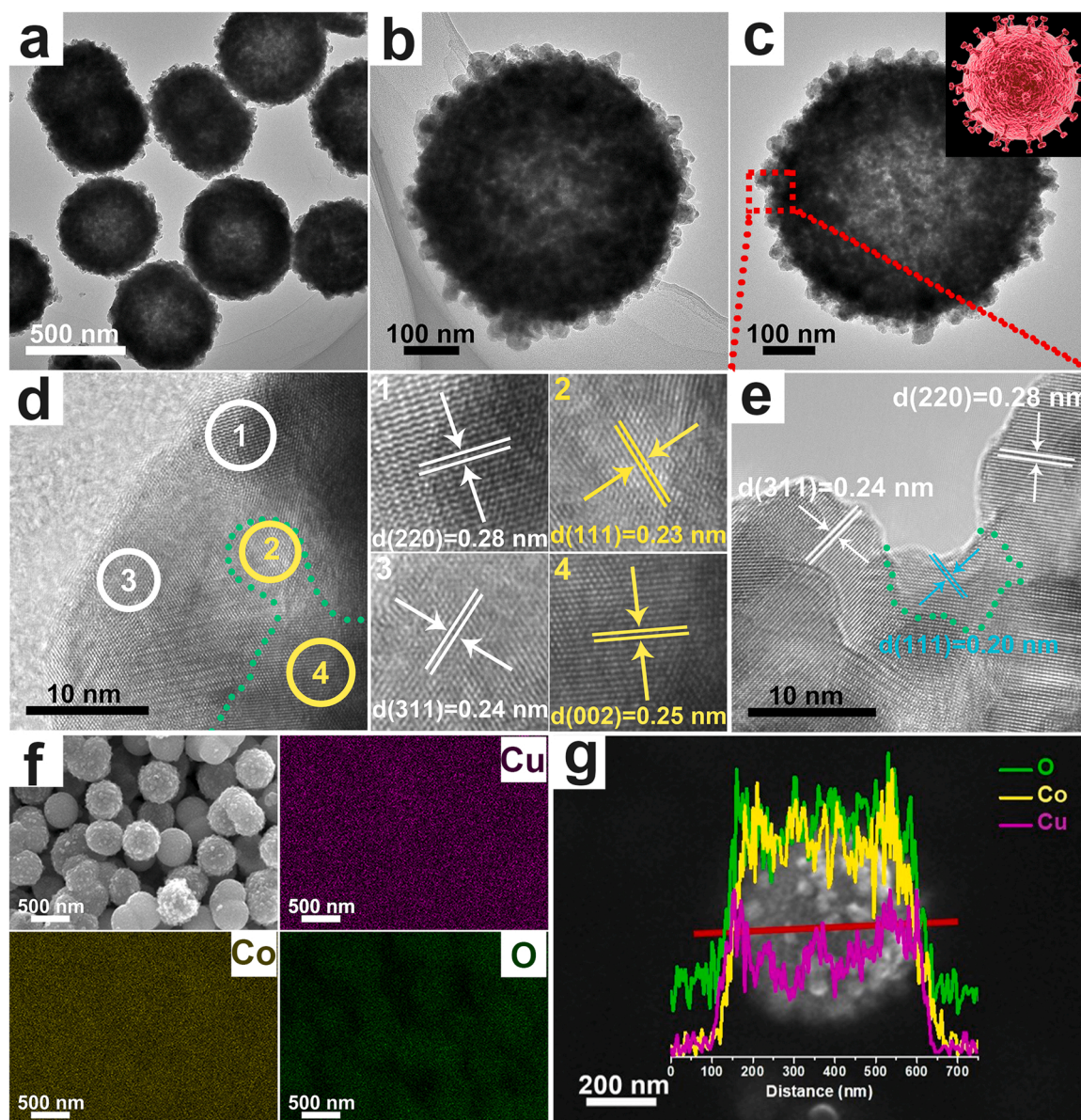

Fig. 2. TEM images of $CuO/Cu_{0.76}Co_{2.24}O_4$ (a, b) and V60 (c), HRTEM images of $CuO/Cu_{0.76}Co_{2.24}O_4$ (d) and V60 (e), elemental mapping (f), and line scan (g) of V60, the inset is schematic diagram of coronavirus.

correspond to the (220) and (311) planes of the $Cu_{0.76}Co_{2.24}O_4$, respectively. And 0.23 and 0.25 nm distance corresponding to (111) and (002) planes of CuO. Besides, there is sufficient contact between the $Cu_{0.76}Co_{2.24}O_4$ and CuO.

Exploration of the $Cu/Cu_{0.76}Co_{2.24}O_4$-V_O morphology revealed that the nanospheres were maintained after the AA reduction, and the surface roughness increased (Fig. S2c, d). But the V90 nanospheres showed significant rupture due to the damage to the microscopic morphology of the long-term AA reduction (Fig. S2f). V60 is also in the shape of a coronavirus-like hollow nanosphere which is similar to CuO/$Cu_{0.76}Co_{2.24}O_4$ (Fig. 2c). Other nanosphere CuO/$Cu_{0.76}Co_{2.24}O_4$ were also prepared by controlling the hydrothermal time (Fig. S3), and the catalytic activity of coronavirus-like hollow nanosphere (hydrothermal time 1 h) was better than other nanosphere catalysts with smooth surface in the AB catalytic reaction (Fig. S4). This indicates that the surface protruding particles of the nanosphere are like the crown-like spike of a virus, which facilitate the adsorption and action process of the catalyst on the reactants. In the HRTEM image of V60 (Fig. 2e), in addition to the crystal plane of $Cu_{0.76}Co_{2.24}O_4$, Cu (111) with an interlayer distance of 0.20 nm can be clearly observed, and no CuO crystal plane appears. All CuO in V60 has been converted to Cu, which is consistent with the results by XRD. The element mapping results in Fig. 2f support the uniform distribution of Co, Cu, and O elements in V60, indicating a homogeneous heterogeneous structure without the accumulation of metallic Cu. In addition, the line scan of individual nanosphere also shows that the elements are uniformly distributed, and the low relatively elemental content in the central part of the sphere is the result of the cavity portion (Fig. 2g).

For the catalyst formation process, the $Cu_{0.76}Co_{2.24}O_4$ hollow nanospheres structure is generated by the technique of self-templating and calcination processes [34], in which Cu^{2+} partially replaces Co^{2+} of the Co_3O_4 spinel structure to form TMOs, while generating small amount of defects (such as Vo) to balance the interior electronic structure. Then, CuO/$Cu_{0.76}Co_{2.24}O_4$ can be formed by adding an excess of Cu^{2+} during the hydrothermal process, with an extremely sufficient contact between the two phases. Through the reduction of CuO/$Cu_{0.76}Co_{2.24}O_4$ by mild AA, CuO is reduced to Cu, while $Cu_{0.76}Co_{2.24}O_4$ forms a V_O-rich structure. Thus, dual-active-sites $Cu/Cu_{0.76}Co_{2.24}O_4$-V_O hollow nanospheres are formed (Scheme 1). Among them, metal and TMOs are respectively the active sites of catalysis.

## 3.2. Variation in the degree of surface defects on catalytic performance

The coordination environment of the catalysts is characterized by Raman spectroscopy (Fig. 3a). The $Cu/Cu_{0.76}Co_{2.24}O_4$-V_O mainly includes 5 characteristic Raman peaks. The peak at 193.5, 519.8, and 619.4 cm^{-1} in the spectra correspond to the F_{2g} mode. The band centered at 193.5 cm^{-1} is the F_{2g} mode of CoO_4 tetrahedral site and 519.8 cm^{-1} is mainly due to the vibration of the Cu–O bond stretching as the Cu^{2+}–O^{2-} in $Cu_{0.76}Co_{2.24}O_4$ [35]. The band at 483.9 cm^{-1} correlates with E_g symmetry and 690.4 cm^{-1} for the A_{1g} mode corresponds to the CoO_6 octahedral site. The A_{1g} mode is most susceptible to structural changes such as lattice defects [36]. The negative shift of the A_{1g} symmetry in $Cu/Cu_{0.76}Co_{2.24}O_4$-V_O indicates the formation of V_O defects in the structure, while the degree of negative shift is listed in Table 2. As

the time of AA treatment grows, the shift degree of A_{1g} peak increases and then shrinks again. V60 has the largest negative shift reflecting the highest defects in it [37]. In addition, the broadening of the A_{1g} peak compared to V0 (same as CuO/$Cu_{0.76}Co_{2.24}O_4$) is due to the disturbed crystal structure and increased defects caused by V_O.

The variation of surface defects in the series of $Cu/Cu_{0.76}Co_{2.24}O_4$-V_O is further explored by O_2-TPD, as shown in Fig. 3b. Generally, the desorption of oxygen species on the surface of the sample undergoes the following process with increasing temperature: $O_2(ads) \rightarrow O_2^-(ads) \rightarrow O^-(ads) \rightarrow O^{2-}(lattices)$ [38]. The surface oxygen species $O_2^-(ads)$ and $O^-(ads)$ are easily adsorbed on the surface defects of the sample such as V_O at a desorption temperature range of 150–700 °C [28]. Compared with V0, the other samples have a larger peak area and a higher desorption temperature for adsorbed oxygen species (O_{ads}), which may indicate stronger adsorption and higher adsorption capacity of V_O. The O_{ads}/O_{latt} ratio reflects the relative content of O_{ads}, which in turn characterizes the change in defect content in the samples. As Table 2, the O_{ads} content increased and then decreased with the reduction treatment time and is the highest in V60, which proves that more V_O was generated in V60 to adsorb reactive oxygen species. The strong oxygen species adsorption ability is conducive to the adsorption of H_2O and intermediate oxygen species in the AB catalysis process. Besides, the release temperature of O_{latt} gradually decreases with the increase of defects content, which clarifies the looseness of the lattice structure after the formation of V_O in the catalyst structure [39].

The surface composition and chemical states of $Cu/Cu_{0.76}Co_{2.24}O_4$-V_O were investigated by XPS (Fig. 3c–f). The XPS survey spectra can be observed with peaks attributed to Cu, Co, O, and C elements, revealing that no other impurities were introduced on the surface during the AA reduction process (Fig. S5). Cu 2p spectra in Fig. 3c consists of two main peaks at about 934 and 953 eV correspond to Cu $2p_{3/2}$ and $2p_{1/2}$ in the catalyst, respectively. The peaks of V0 at 934.4 and 954.0 eV correspond to Cu^{2+}, while the peaks of other samples at 933.2 and 952.8 eV correspond to Cu^0 [40,41]. The content of Cu^0 increase as the reduction time and remains constant at about 28.8% in V60 and V90 (Fig. 3f). It can be deduced that the CuO in CuO/$Cu_{0.76}Co_{2.24}O_4$ is 12.2 wt%, which has a similar value to the refined results by XRD (14.2 wt%). The Cu 2p spectra of single-phase $Cu_{0.76}Co_{2.24}O_4$ and $Cu_{0.76}Co_{2.24}O_4$-V60 exhibit only Cu^{2+} peaks and no chemical state changes during the reduction process (Fig. S6b). The reduction treatment resulted in the gradual reduction of CuO to Cu, while Cu^{2+} in the $Cu_{0.76}Co_{2.24}O_4$ structure remained unchanged.

Besides, the two main peaks of Co 2p spectra at 780 and 795 eV are $2p_{3/2}$ and $2p_{1/2}$, respectively (Fig. 3d). There could be deconvoluted into two kinds of Co species, since Co^{2+} is more stable than Co^{3+}, including Co^{3+} with binding energies at 779.8 and 794.9 eV and Co^{2+} at 781.3 and 796.6 eV [42]. The change of Co^{2+} content can be observed in Fig. 3f that $Cu/Cu_{0.76}Co_{2.24}O_4$-V_O is significantly higher than CuO/$Cu_{0.76}Co_{2.24}O_4$, and it gradually increases as the reduction treatment time. And the Co^{2+} content in V60 is higher than other samples, reaching 67.9%. However, the decrease in Co^{2+} of V90 is due to the corrosion effect with long-term reduction treatment process leading to its microstructural rupture (Fig. S2f) [28,43,44]. Additionally, three O species are existing fitted to the O 1s spectra, located at 529.8, 531.6, and 533.1 eV, corresponding to lattice oxygen (M–O), vacant oxygen (V_O), and adsorbed
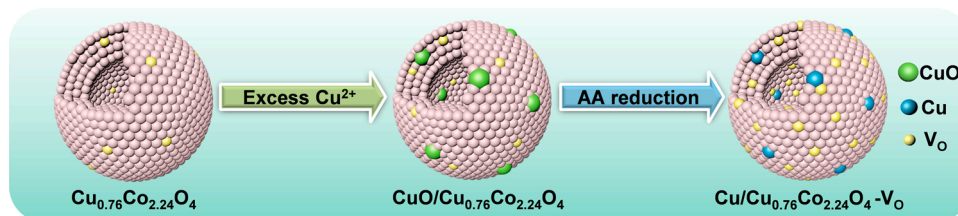
Scheme 1. Schematic illustration of preparing the $Cu/Cu_{0.76}Co_{2.24}O_4$-V_O hollow nanospheres.
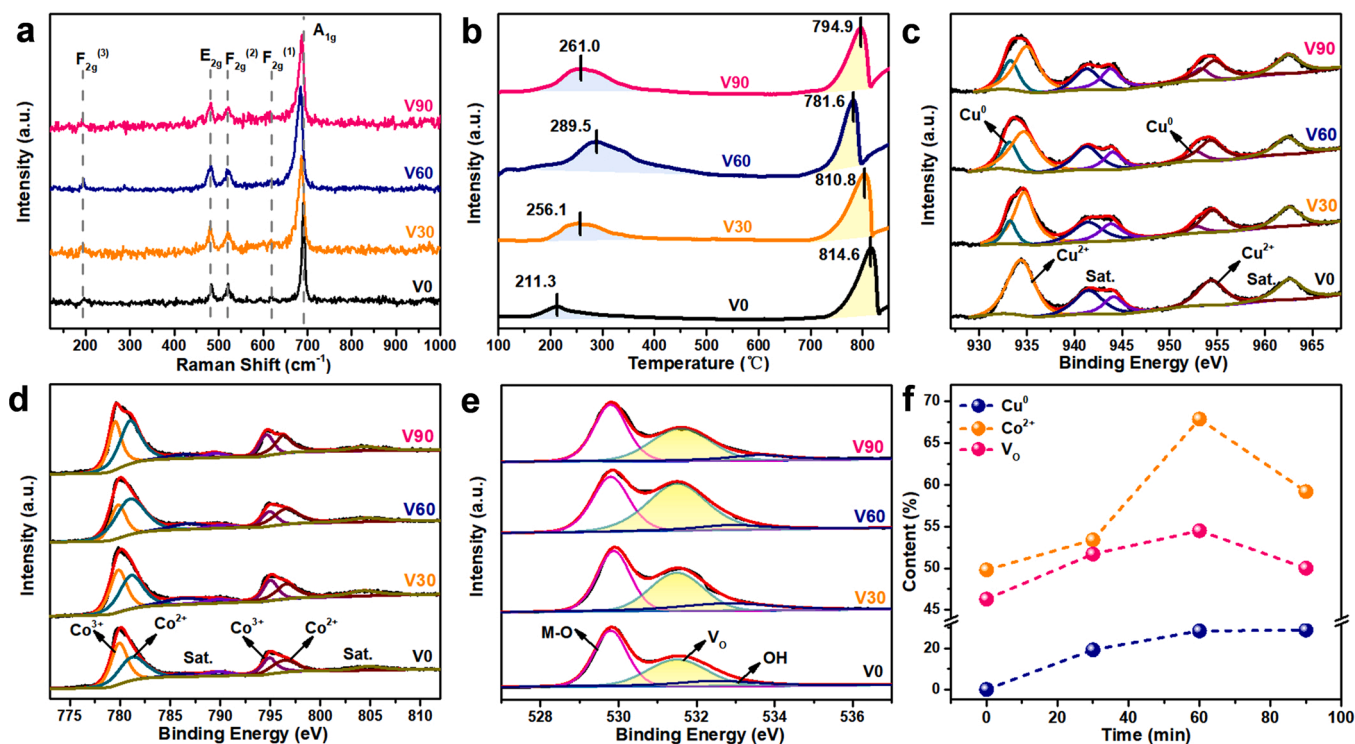
Fig. 3. Raman spectra (a) and O_2-TPD profiles (b) of $Cu/Cu_{0.76}Co_{2.24}O_4$-V_O, XPS spectra of Cu 2p (c), Co 2p (d), and O 1s (e), and changes of Cu^0, Co^{2+} and V_O content in $Cu/Cu_{0.76}Co_{2.24}O_4$-V_O (f).

Table 2
Raman and O_2-TPD parameters of $Cu/Cu_{0.76}Co_{2.24}O_4$-V_O.

Sample	λ (cm^{-1})	O_{ads}/O_{latt}
V0	0	0.281
V30	4.3	0.540
V60	6.1	1.603
V90	2.7	0.940

hydroxyls (OH), respectively (Fig. 3e) [33]. The V_O content is calculated by comparing the peak area of V_O to the sum of the peak areas of M–O and V_O. V_O in $Cu/Cu_{0.76}Co_{2.24}O_4$-V_O has a great increase compared to V0, which has the same trend as the Co^{2+} content (Fig. 3f). Besides, the V_O in V60 can reach up to 53.5% making $Cu/Cu_{0.76}Co_{2.24}O_4$ a V_O-rich structure. Although the CuO reduction treatment also drives V_O (Fig. S7), the CuO content in the heterogeneous structure is small and dispersed, and the content of Co^{2+} and V_O in the single-phase structure of $Cu_{0.76}Co_{2.24}O_4$-V60 also is comparable to that in V60 (Fig. S6c and d, Table S1), so it can be assumed that the V_O of the heterostructure are basically derived from $Cu_{0.76}Co_{2.24}O_4$. During the AA treatment, the degree of V_O defects on the surface of $Cu/Cu_{0.76}Co_{2.24}O_4$ increased, showing a volcanic trend, consistent with the characterization results of Raman and O_2-TPD. After 60 min of AA treatment, the content of Co^{2+} and V_O in $Cu/Cu_{0.76}Co_{2.24}O_4$ is the highest, the electron density around the Co elements in $Cu_{0.76}Co_{2.24}O_4$ increased the most, and these enriched electrons are beneficial to the attack on H_2O molecules during the hydrolysis of AB.

In addition, the specific surface area (SSA) of V60 increases, and the characteristic pore diameter does not change significantly, only showing an increase in pore volume (Fig. S8). It indicates that the AA reduction increased the number of pores or pore length in the catalyst, which is more favorable for the catalytic process of reactant transfer and thus accelerated the catalytic reaction [45]. The above characterizations of $Cu/Cu_{0.76}Co_{2.24}O_4$-V_O indicate that the catalyst forms a series of surface with varying degrees of defects by the AA treatment time, with the

highest increase in electron density around Co and the strongest adsorption of oxygen species when the defects is highest.

The catalytic performances of catalysts with different V_O contents for hydrogen generation from AB were tested (Fig. 4). The volume of hydrogen released by the catalytic hydrolysis of all catalysts was close to the theoretical. As shown in Fig. 4a, it takes a long activation period for V0 to produce hydrogen in the catalytic reaction. And the activation period required for the reaction catalyzed by $Cu/Cu_{0.76}Co_{2.24}O_4$-V_O decreases as the reduction treatment time increases, and remained basically unchanged to V60 and V90. This is due to the fact that the time required for the reduction of CuO to metallic Cu by AB with different ratios of Cu: CuO in $Cu/Cu_{0.76}Co_{2.24}O_4$-V_O. The CuO in the V60 and V90 catalysts has been completely reduced to metallic Cu, the activation time of the catalytic hydrolysis reaction is basically close, and hydrogen is generated almost without activation period. However, in the catalytic reaction, hydrogen needs to reach a certain amount of accumulation before it can escape from the surface of the reaction solution to be monitored. Different catalytic rates affect the accumulation time, so there is a slight difference in the no-hydrogen generation time between V60 and V90. The activation period remains constant in the catalytic reaction of pure $Cu_{0.76}Co_{2.24}O_4$-V_O due to the absence of reduction to produce metallic Cu (Fig. S9). The calculation of TOF values for the $Cu/Cu_{0.76}Co_{2.24}O_4$-V_O catalyzed hydrolysis reaction (Fig. 4b) reveals that the TOF values also show a volcano-type trend as the AA treatment time increases, which is the same trend as the defect content contained therein. Similarly, the TOF values of $Cu_{0.76}Co_{2.24}O_4$-V_O and mechanically mixed catalysts of CuO and $Cu_{0.76}Co_{2.24}O_4$-V_O also shows a trend of first increasing and then decreasing with reduction time (Fig. 4b), but all lower than that of $Cu/Cu_{0.76}Co_{2.24}O_4$-V_O, indicating that V_O have a general effect of the catalyst activity and also reflects the optimization effect of the heterostructure on the catalytic reactions. As shown in the Fig. 4c, as the content of Co^{2+} determined by XPS increases, the TOF value of the catalytic reaction gradually increases. The V60 exhibits the highest TOF and reached 28.46 $mol_{H2}/(mol_{cat}·min)$, 45.9 times of Cu (0.62 $mol_{H2}/(mol_{cat}·min)$) (Fig. 4d). Therefore, the enrichment of
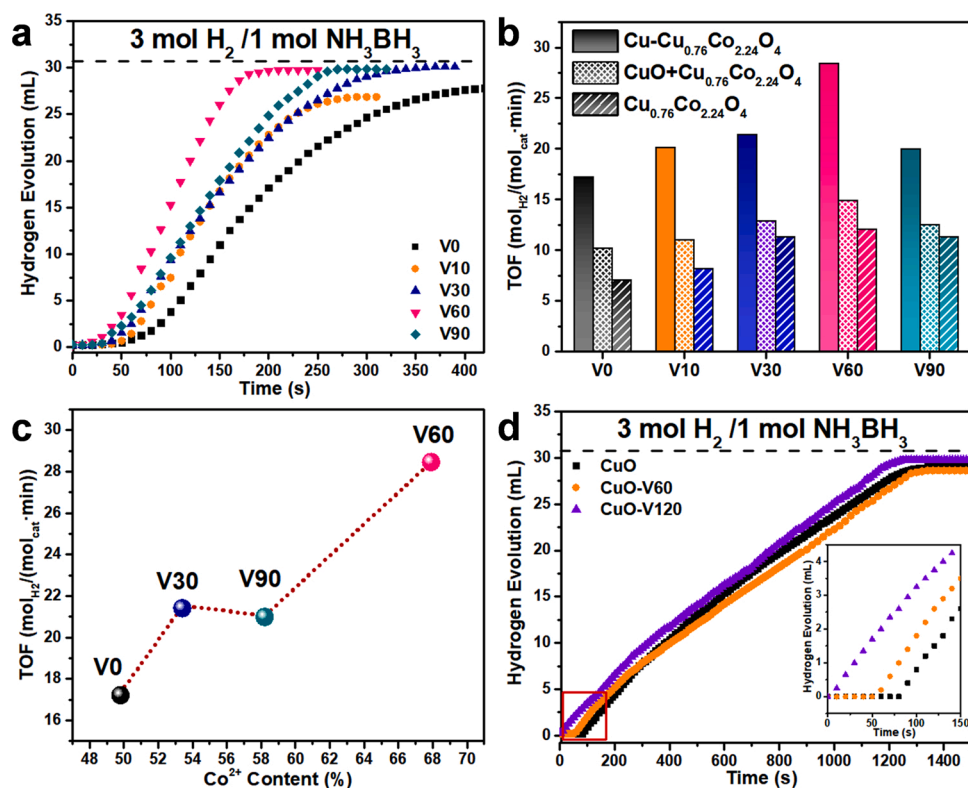
Fig. 4. Time-course plots for hydrogen generation from the dehydrogenation of AB by Cu/$Cu_{0.76}Co_{2.24}O_4$-V_O (a) and CuO-Vt (d), and the corresponding TOF value of Cu/$Cu_{0.76}Co_{2.24}O_4$-V_O, mechanically mixed CuO and $Cu_{0.76}Co_{2.24}O_4$-V_O (CuO+$Cu_{0.76}Co_{2.24}O_4$) with CuO 14.2 wt%, and $Cu_{0.76}Co_{2.24}O_4$-V_O (b) (AB = 0.45 mmol, m[cat.]/m[AB] = 0.571, H_2O = 10 mL, T = 25 °C), and Cu/$Cu_{0.76}Co_{2.24}O_4$-V_O catalytic activity changes with Co^{2+} content determined by XPS (c), the insert is the enlargement of the boxed-out part of the (d).

electrons around Co caused by the increased content of Vo defects in the Cu/$Cu_{0.76}Co_{2.24}O_4$-V_O catalyst has a significant enhanced the catalytic activity and exhibits at a shorter activation period. In addition, the heterostructure can significantly improve the catalytic efficiency is also reflected by the lower TOF values of $Cu_{0.76}Co_{2.24}O_4$-V_O and mechanically mixed catalysts than the metal/TMOs structure.

The ratios of CuO to Cu in Cu/$Cu_{0.76}Co_{2.24}O_4$-V_O is different, which is illustrated by XRD and XPS characterization. The catalytic activities of CuO and CuO-Vt shows that the ratio of CuO/Cu basically did not affect the hydrolysis activity, but only the activation period of the hydrolysis reaction (Fig. 4d). And the activation period gradually reduced as the proportion of Cu increased. Therefore, the Cu/$Cu_{0.76}Co_{2.24}O_4$-Vo catalyst activity is not affected by ratio of Cu/CuO, but by the content of surface V_O.

3.3. Enhancement of catalytic performance by heterostructures

Since CuO/$Cu_{0.76}Co_{2.24}O_4$ requires a longer activation period for the hydrolysis reaction, samples after the activation period of catalytic reaction were characterized to demonstrate the changes in the CuO/$Cu_{0.76}Co_{2.24}O_4$. The phase structure of the activation period sample is a mixed phase of Cu and $Cu_{0.76}Co_{2.24}O_4$, and the diffraction peak of $Cu_{0.76}Co_{2.24}O_4$ is not shifted (Fig. S10a, b). The microscopic morphology of the hollow nanospheres is maintained and only the crystal plane of $Cu_{0.76}Co_{2.24}O_4$ and Cu could be observed by HRTEM (Fig. S10c, d). The surface chemical state was precisely determined by XPS (Fig. S11). The Co 2p spectra showed that the proportion of Co^{2+} remained slightly elevated, but the V_O content did not change significantly after the activation period (Table S1). Meanwhile, the Cu 2p spectra of activation period sample exhibits a mixed-valence of Cu^{2+} with Cu^0 and the Cu^0 content is consistent with that in V60, so it can be suggested that the activation period causes a complete reduction of CuO to Cu. Therefore, it can be explained that during the activation period, the reduction of AB only reduces CuO to Cu, and there are no more defects generated in $Cu_{0.76}Co_{2.24}O_4$. In addition, the SSA of activation period sample is

51.38 m^2/g, the characteristic pore size is 3.1 nm, and the pore volume is 0.123 cm^3/g (Fig. S12), which are all close to V60, so the increase of the SSA of V60 compared to V0 is mainly due to the reduction of CuO to Cu.

The role of the component content in the heterogeneous structure of Cu and $Cu_{0.76}Co_{2.24}O_4$ on the catalytic performance can be reflected by investigating the hydrolysis performance of different CuO contents in CuO/$Cu_{0.76}Co_{2.24}O_4$. The CuO/$Cu_{0.76}Co_{2.24}O_4$ catalysts with different CuO contents were obtained by adding different ratios of Co:Cu in the synthesis process. The variation of the peak intensity of CuO (002) plane at $2\theta = 35.5°$ and $Cu_{0.76}Co_{2.24}O_4$ (311) plane at $2\theta = 36.8°$ in the XRD patterns can be judged that the CuO content in CuO/$Cu_{0.76}Co_{2.24}O_4$ gradually increases with the Cu addition (Fig. 5a, b). Similarly, the results of SEM-EDS also showed that the ratio of Co:Cu in CuO/$Cu_{0.76}Co_{2.24}O_4$ increased, that is, the content of CuO increased (Fig. S13). As shown in Fig. 5c, the hydrolysis catalytic performance tests on CuO/$Cu_{0.76}Co_{2.24}O_4$ revealed that all catalysts need the activation period of the reaction, which is caused by the AB reduction of CuO. The TOF value of the CuO/$Cu_{0.76}Co_{2.24}O_4$ catalyzed reaction has a volcano-type trend of increasing and then decreasing with Cu content, and CuO/$Cu_{0.76}Co_{2.24}O_4$ exhibited a TOF value of 18.63 mol_{H2}/(mol$_{cat}$·min) with the Co:Cu = 2:1 (Fig. 5d).

Catalysts with simple mechanical mixing of CuO with $Cu_{0.76}Co_{2.24}O_4$, exhibiting similar nanosphere morphology with a diameter of about 530 nm (Fig. S14). By comparing the catalytic activity of mechanically mixed CuO and $Cu_{0.76}Co_{2.24}O_4$ catalysts with different CuO contents (Fig. 5e), it can be found that the activation period of mechanically mixed catalysts is longer than heterogeneous structures, which is due to the fact that CuO is not well dispersed in the catalyst to make sufficient contact with AB and thus take a long time for reduction. Also, the TOF values of the mechanically mixed samples are significantly lower than CuO/$Cu_{0.76}Co_{2.24}O_4$ (Fig. 5f), indicating the importance of the enhanced performance of the interactions formed by the tight junctions of the bi-phases in the heterogeneous. The TOF of mechanically mixed samples also has a volcanic change trend with CuO content.
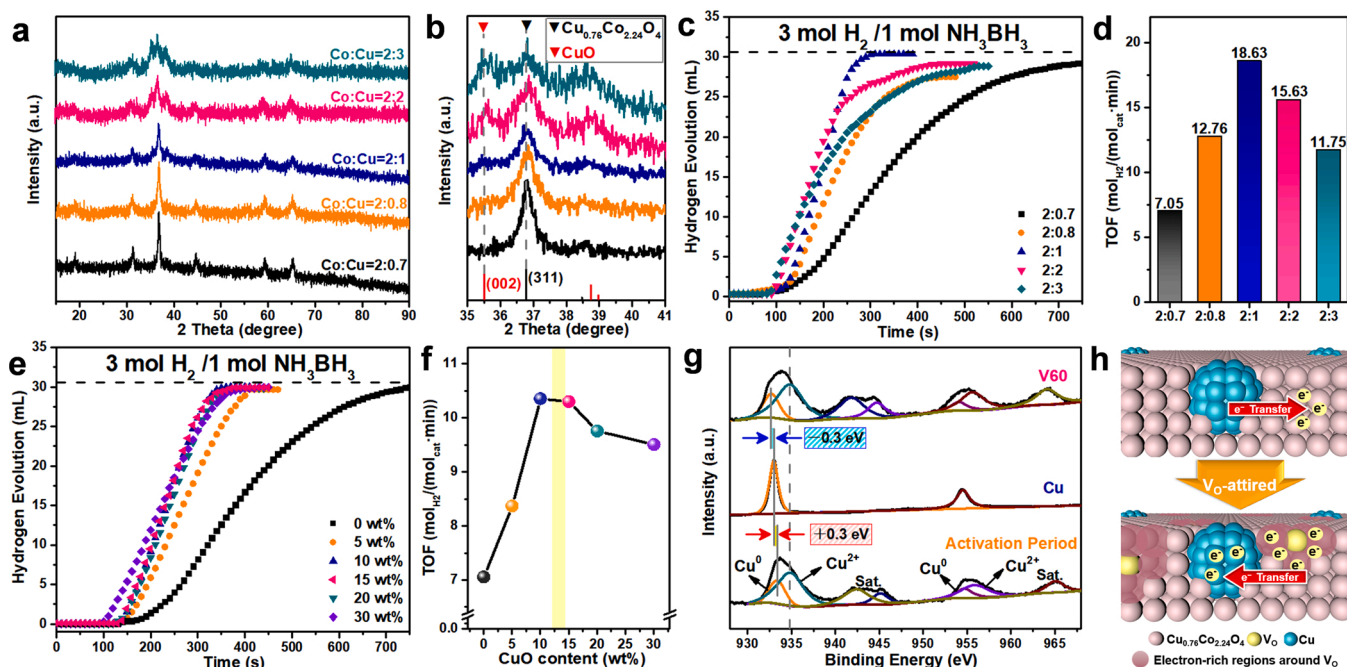
Fig. 5. XRD patterns of CuO/$Cu_{0.76}Co_{2.24}O_4$ with different Co:Cu molar ratio (a, b). Time-course plots for hydrogen generation from the dehydrogenation of AB by CuO/$Cu_{0.76}Co_{2.24}O_4$ with different Co:Cu molar ratio (c) and mechanically mixed CuO and $Cu_{0.76}Co_{2.24}O_4$ with different Cu content (e), and the corresponding TOF value of each reaction (d, f) (AB = 0.45 mmol, m[cat.]/m[AB] = 0.571, H_2O = 10 mL, T = 25 °C). XPS spectra of Cu 2p of catalysts (g) and the V_O defect construction strategy regulates the direction of electron transfer between Cu and $Cu_{0.76}Co_{2.24}O_4$, both of which are active sites (h).

The TOF value (10.45 mol_{H2}/(mol_{cat}·min)) is the highest when the content is in the range of 10–15 wt%. In the previous refinement characterization, we proved that the CuO content in CuO/$Cu_{0.76}Co_{2.24}O_4$ was about 14% (yellow band in Fig. 5f), which is basically consistent with the optimal content of the mechanically mixed sample. So, it is shown that the synergistic effect of Cu and $Cu_{0.76}Co_{2.24}O_4$ can be best exploited in the heterogeneous structure in appropriate proportions. At this time, the metallic Cu content is calculated to be 11.35 wt% through the calculation of the refinement results.

In order to determine the interaction between Cu and $Cu_{0.76}Co_{2.24}O_4$ in heterostructures, the electron transfer on the surface of the element was investigated. Through the above discussion, it has been clearly determined that Co^{2+} content in the both Cu/$Cu_{0.76}Co_{2.24}O_4$ -V_O and CuO/$Cu_{0.76}Co_{2.24}O_4$ after the activation period increased, indicating that $Cu_{0.76}Co_{2.24}O_4$ surface in the heterostructure is electron-rich compared to pure $Cu_{0.76}Co_{2.24}O_4$. The surface electron density of $Cu_{0.76}Co_{2.24}O_4$ in V60 increases the most because of the existence of V_O. Besides, the change of electron density around Cu in the heterostructure is determined by comparison with single metallic Cu (Fig. 5g). First, the positions of the Cu^{2+} peaks in all catalysts have not shifted, so the electron density around Cu^{2+} in the $Cu_{0.76}Co_{2.24}O_4$ is maintained. Compared with pure metallic Cu, the binding energy of Cu^0 in the Cu/$Cu_{0.76}Co_{2.24}O_4$ formed after the activation period shifts 0.3 eV to the direction of higher binding energy, indicates the reduced surface electron density. This also shows that the increase of Co^{2+} in $Cu_{0.76}Co_{2.24}O_4$ after the induction period comes from the strong interaction to transfer electrons from Cu to $Cu_{0.76}Co_{2.24}O_4$. Then in V60 with more V_O, the peak position of Cu^0 is shifted toward the lower binding energy, so its electron density increases instead. After the formation of a lot of V_O in $Cu_{0.76}Co_{2.24}O_4$, the elevated electron density is transferred to Cu, with which it has a close interaction (Fig. 5h). These electron transfers fully explain the sufficient interaction of Cu with $Cu_{0.76}Co_{2.24}O_4$ heterostructure and the regulation of the surface electron density of the active site by the attired by V_O. For Cu/$Cu_{0.76}Co_{2.24}O_4$, it is unfavorable to the attacking power of Cu in the catalyst when it transfers electrons into $Cu_{0.76}Co_{2.24}O_4$, while the V_O modification increases the Cu surface

electrons while ensuring $Cu_{0.76}Co_{2.24}O_4$ surface has an electron-rich state, which facilitates the attack on reactants.

Besides, the durability performance of V60 was tested (Fig. S15a). V60 only maintained 43.1% of the original TOF value after five times of reuse. The XRD characterization of the used V60 shows that only the diffraction peaks of Cu (111) and $Cu_{0.76}Co_{2.24}O_4$ (311) crystal plane appear (Fig. S15b), indicating that the catalyst maintains the mixed-phase structure of Cu and $Cu_{0.76}Co_{2.24}O_4$. However, the hollow nanospheres are apparently surrounded by flocculent material (Fig. S15c, d), which seriously hinders the contact between the catalyst and the reactants. And flocculent materials make the crystal plane difficult to be probed, thus weakening the diffraction peak intensity. The valence environment of V60 after used was analyzed by XPS characterization (Fig. S16). The valence states of Cu and Co and the content of V_O in the catalyst did not change significantly, indicating that the structure of the catalyst was well maintained after the catalytic reaction, but peaks of B and N elements appeared at 192.1 and 399.9 eV for adsorption of BO^{2-} and N–H species on the catalyst surface which indicates the presence of hydrolysis by-products. At the same time, the FTIR test also showed that there are vibration peaks of B–O bond in addition to M–O bond (Fig. S16f). The above shows that the structure and morphology of the catalyst did not change significantly after being used, and the performance degradation is mainly due to the coverage of the surface by the by-products.

3.4. Mechanism of Cu/$Cu_{0.76}Co_{2.24}O_4$-V_O for enhanced activity

The cleavage of the O–H bond in H_2O molecules has been demonstrated in several studies as an RDS in the hydrolysis reaction of AB [46, 47]. In order to verify this reality, tritium water (D_2O) was used to conduct kinetic isotope effect (KIE) experiments. Fig. S17 shows the CuO/$Cu_{0.76}Co_{2.24}O_4$ catalyzed hydrolyze AB using H_2O and D_2O, respectively. The hydrogen production rate in D_2O is significantly lower than H_2O. The KIE (H_2O rate/ D_2O rate) is also calculated to be 2.78 (Fig. 6b), confirming that H_2O cleavage is RDS of AB dehydrogenation reaction. For V60, the rate of hydrogen generation in D_2O decreased
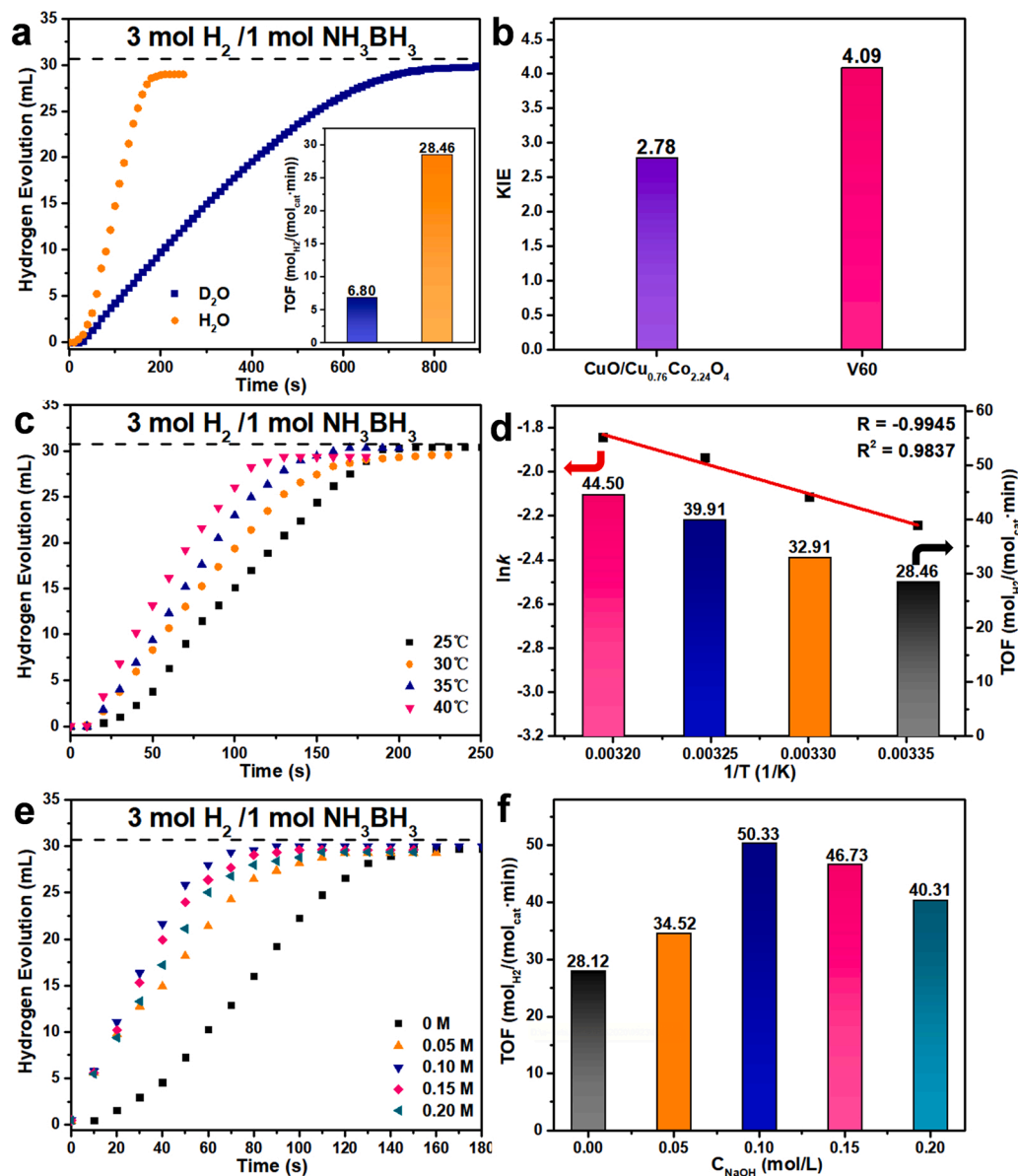
Fig. 6. Time-course plots for hydrogen generation from the dehydrogenation of AB by V60 in H_2O and D_2O (a) and KIE values of $CuO/Cu_{0.76}Co_{2.24}O_4$ and V60 (b) (AB = 0.45 mmol, m[cat.]/m[AB] = 0.571, H_2O = 10 mL, T = 25 °C), time-course plots for hydrogen generation from the dehydrogenation of AB by V60 under different test temperatures (c) (T = 25, 30, 35 and 40 °C) and Arrhenius plots and TOF values (d), time-course plots for hydrogen generation from the dehydrogenation of AB by V60 with different NaOH concentration (e) and TOF values (f) (c_{NaOH} = 0, 0.05, 0.10, 0.15, 0.20 M).

more pronounced, with a higher KIE value of 4.09 (Fig. 6a, b). It is confirmed that compared with $CuO/Cu_{0.76}Co_{2.24}O_4$, V60 significantly accelerates the cleavage of O–H bonds in H_2O molecules [18,48]. The accelerated O–H bond cleavage increases the rate of the catalytic reaction, which indicates that the presence of V_O in V60 is very favorable for the adsorption and activation of H_2O to promote the hydrolysis reaction.

To better understand the role of V_O in the $Cu_{0.76}Co_{2.24}O_4$ catalyst, the kinetic analysis was carried out. The V60 catalytic hydrolysis reaction test at different temperatures is shown in Fig. 6c. According to the Arrhenius plots, the activation energy (E_a) value of V60 was calculated to be 24.36 kJ/mol (Fig. 6d), lower than that of $CuO/Cu_{0.76}Co_{2.24}O_4$ (30.60 kJ/mol) (Fig. S18), and significantly lower than that of most of the non-noble metal catalysts reported in the literature (Table S2). This indicates that the catalyst with V_O attired promotes the dissociation process of reactant molecules, significantly reducing the energy barrier for catalytic hydrolysis and speeding up the rate.

Fig. 6e and f show the catalytic activities of V60 with the addition of NaOH as a catalyst promoter. Obviously, among different NaOH concentrations, V60 catalyzed the highest rate of AB hydrolysis at a concentration of 0.10 M, with a TOF value could reach 50.33 mol_{H2}/(mol_{cat}·min), which exceeded many catalysts with non-noble metals

(Table S2). OH^- provided by NaOH is beneficial to increase the electron density on the catalyst surface and facilitates the oxidative addition reaction of H_2O [41,49]. However, the excess of OH^- concentration may cover the active site and hinder the coordination of *H and H_2 dissociation process. Furthermore, the increase of catalyst rate in NaOH solution further indicates that the RDS in the hydrolysis reaction is the cleavage of the O–H bond in H_2O.

To further determine the reasons for the excellent catalytic activity, DFT calculations were performed for $Cu/Cu_{0.76}Co_{2.24}O_4$ and $Cu/Cu_{0.76}Co_{2.24}O_4-V_O$ to explore the feasibility of catalytic active sites and V_O for effective catalyst performance enhancement, respectively. The catalytic performance of the catalyst was evaluated by estimating the adsorption energy (ΔE_{ads}) and activation energy barriers of H_2O and AB molecules. The adsorption and activation of AB and H_2O on the representative Cu (111) and $Cu_{0.76}Co_{2.24}O_4$ (311) surfaces, as the thermodynamically stable and most exposed facets. A recent study has shown that Co centers with octahedral geometry are more active toward the adsorption of H_2O near V_O in the surface to fulfill the coordination number of six [50]. Therefore, The Co atom is selected as the active site for $Cu_{0.76}Co_{2.24}O_4$ catalysis. The optimized most stable adsorption configurations of the relevant species on the Cu and $Cu_{0.76}Co_{2.24}O_4$

surfaces are presented in Fig. S19, and the corresponding potential energy curves are shown in Fig. 7a, b, respectively. From the perspective of the kinetic, the activation barrier of the H_2O molecule on the Cu surface (1.54 eV) is higher than the $Cu_{0.76}Co_{2.24}O_4$ surface (1.27 eV). while the activation energy barrier of AB molecule (Cu (1.06 eV) < $Cu_{0.76}Co_{2.24}O_4$ (1.39 eV)) is lower. This shows that $Cu_{0.76}Co_{2.24}O_4$ has a stronger ability to activate H_2O molecules during AB hydrolysis, meanwhile, Cu is more favorable for AB molecules to produce H*. Therefore, it suggests that the formation of Cu and $Cu_{0.76}Co_{2.24}O_4$ heterogeneous structures allows the metal and TMO to be used as active sites to enhance the catalyst activity, respectively.

As for the adsorption of reactants on the surface of Cu/$Cu_{0.76}Co_{2.24}O_4$ (Fig. 7c), the ΔE_{ads} of H_2O molecules on the $Cu_{0.76}Co_{2.24}O_4$ (311) surface (−1.256 eV) is lower than that on the Cu (111) surface (−0.671 eV), and the ΔE_{ads} of AB on Cu (111) (−0.852 eV) is significantly lower than that of $Cu_{0.76}Co_{2.24}O_4$ (311) (−0.511 eV), indicating that the Cu in the Cu/$Cu_{0.76}Co_{2.24}O_4$ is still easy to adsorb AB, and TMOs is facilitated to act on H_2O molecule. it is thus demonstrated that the metal/TMOs heterostructure can act as a dual-active-sites catalyst for hydrolysis of AB. In addition, the activation barrier of $Cu_{0.76}Co_{2.24}O_4$ to H_2O (0.75 eV) and Cu to AB (1.00 eV) in Cu/$Cu_{0.76}Co_{2.24}O_4$ are lower than that of single-phase $Cu_{0.76}Co_{2.24}O_4$ and Cu, respectively. It shows that the Cu/$Cu_{0.76}Co_{2.24}O_4$ heterostructure can promote the activation of reactant molecules in the catalytic process, especially the activation of H_2O molecules by $Cu_{0.76}Co_{2.24}O_4$, but the effect of Cu on AB molecules is not significantly enhanced.

To simplify the calculation process, we constructed three ideal Cu/$Cu_{0.76}Co_{2.24}O_4$ models: where the $Cu_{0.76}Co_{2.24}O_4$ surface V_O concentrations are respectively the surface without V_O, with one (V_{O1}) and two (V_{O2}) V_O. It must be noted that the modeled V_O is only theoretical and does not represent the actual V_O concentration of the sample. Cu/$Cu_{0.76}Co_{2.24}O_4$-V_{O1} and Cu/$Cu_{0.76}Co_{2.24}O_4$-V_{O2} activate H_2O molecule during hydrolysis (Fig. S20), and the activation barriers of H_2O molecule are 0.57 and 0.48 eV, respectively, which are lower than those of Cu/$Cu_{0.76}Co_{2.24}O_4$ base (Fig. 7d). This finding suggests that the increasing of V_O content in Cu/$Cu_{0.76}Co_{2.24}O_4$ reduces the activation barriers of H_2O on the TMOs surface, due to the low coordination metal sites generated by V_O. For the activation of B–H in AB (Fig. S21), the activation energy barriers of Cu to AB on Cu/$Cu_{0.76}Co_{2.24}O_4$-V_{O1} and Cu/$Cu_{0.76}Co_{2.24}O_4$-V_{O2} are 0.57 and 0.44 eV, respectively, which are much lower than the barrier of Cu/$Cu_{0.76}Co_{2.24}O_4$ (Fig. 7e). While the V_O optimizes the TMOs to reduce the activation energy barrier, the barrier of Cu for AB is also reduced because of the optimized electronic structure of the $Cu_{0.76}Co_{2.24}O_4$-V_O.

The AB hydrolysis process mainly includes five steps (Scheme 2): (i) the adsorption of H_2O and AB on the surface of $Cu_{0.76}Co_{2.24}O_4$-V_O and Cu in the catalyst, respectively; (ii) the O–H bond of H_2O is activated by electrons on the surface of $Cu_{0.76}Co_{2.24}O_4$-V_O and broken to generate H*, at the same time, the B–H bond is activated by metal Cu; (iii) HO* generated by the activation of H_2O molecules attacks AB to break the B–H bond to release H* and formed NH_3–BH_2OH; (iv) two H* released by H_2O and AB combine to generate 1 mol H_2 overflow, and the second

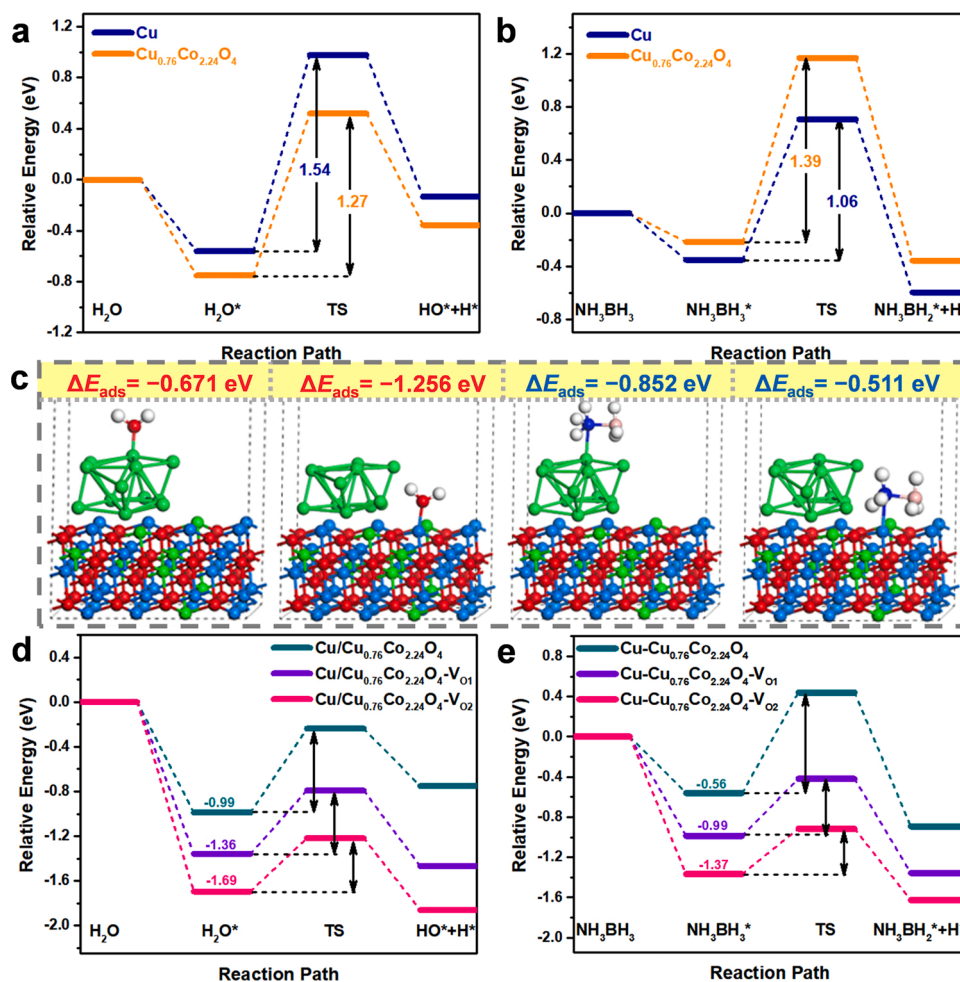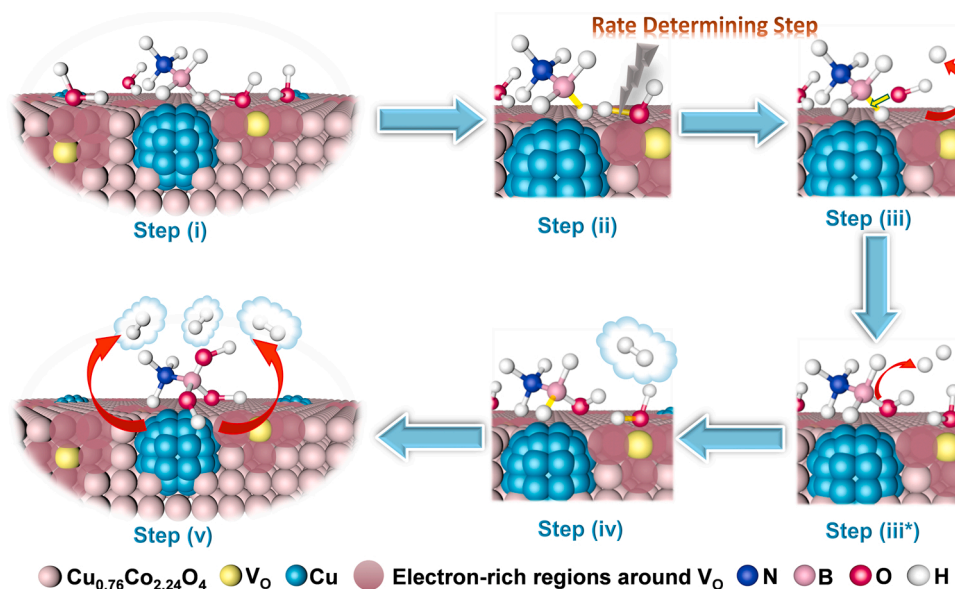**Fig. 7.** Energy profiles of H_2O (a) and AB (b) adsorption and dissociation on Cu (111) and $Cu_{0.76}Co_{2.24}O_4$ (311) facets, ΔE_{ads} of the H_2O and AB molecule on Cu (111) and $Cu_{0.76}Co_{2.24}O_4$ (311) of Cu/$Cu_{0.76}Co_{2.24}O_4$ models surfaces (c), and energy profiles of H_2O (d) and AB (e) adsorption and dissociation of Cu/$Cu_{0.76}Co_{2.24}O_4$ and Cu/$Cu_{0.76}Co_{2.24}O_4$-V_O, respectively.

Scheme 2. A proposed mechanism for AB hydrolysis over $Cu/Cu_{0.76}Co_{2.24}O_4$-V_O.

H_2O molecule is adsorbed around the V_O for activation; (v) after that, the second HO* generated by the second H_2O to attack B–H, and then repeat the above steps until 3 mol H_2 is released. KIE experiment clearly determined that the RDS of the reaction is the breaking of the O–H bond. Combined with the catalyst characterization and theoretical calculation results, V_O in $Cu/Cu_{0.76}Co_{2.24}O_4$-V_O acts as an electron donor to produce electron-rich regions around it, while the electron density on the Cu surface increases due to the electron transfer between the hetero-structures. Therefore, during the catalytic process, $Cu_{0.76}Co_{2.24}O_4$-V_O facilitates the adsorption of H_2O and reduces its reaction energy barrier. At the same time, Cu enhances the adsorption and activation process of AB which accelerates the H* of the B–H release process. The efficient H* generation process accelerates the hydrogen release rate in the catalytic reaction. Thus, the $Cu/Cu_{0.76}Co_{2.24}O_4$-V_O catalyst acts as a dual-active-sites catalyst, in which Cu and $Cu_{0.76}Co_{2.24}O_4$-V_O effectively activate AB and H_2O molecules, respectively, thereby reducing the energy barrier of the entire catalytic reaction and provide excellent catalytic activity.

4. Conclusion

In summary, the V_O attired $Cu/Cu_{0.76}Co_{2.24}O_4$ dual-active-sites catalyst was prepared by simple AA reduction of $CuO/Cu_{0.76}Co_{2.24}O_4$. Various characterization demonstrated the presence of metal/TMOs tight structures and to determine the variation in the content of V_O in the catalysts. The combination of performance tests, kinetic, and DFT calculation analysis demonstrated that the $Cu/Cu_{0.76}Co_{2.24}O_4$-V_O catalysts exhibit better catalytic activity up to 28.46 $mol_{H2}/(mol_{cat}\cdot min)$ at higher content of V_O, which is 45.9 times that of pure Cu. $Cu_{0.76}Co_{2.24}O_4$-V_O in $Cu/Cu_{0.76}Co_{2.24}O_4$-V_O as an active site can effectively activate H_2O molecules, especially enhancing the activation of the O–H bond, which can speed up the RDS of the hydrolysis reaction. This is due to the high content of V_O enriches the Co of $Cu_{0.76}Co_{2.24}O_4$ with electrons, which enhances the adsorption of H_2O, reduces the reaction energy barrier of O–H bond. In addition, Cu surface electrons are enriched by electron transfer between Cu and $Cu_{0.76}Co_{2.24}O_4$-V_O, which accelerates the cleavage of the B–H bond in the catalytic reaction. Overall, the dual-active-sites $Cu/Cu_{0.76}Co_{2.24}O_4$-V_O catalyst provided in this paper effectively accelerates the release rate of active H* in catalytic AB hydrolysis reaction. This report not only shows $Cu/Cu_{0.76}Co_{2.24}O_4$-V_O as an efficient catalyst for AB hydrolysis, but also reasonably explains the metal/TMOs catalytic mechanism, which provides a reliable and enhanced way for the rational design the active sites of non-noble metal

catalysts.

CRediT authorship contribution statement

Chenyang Wang: Methodology, Formal analysis, Writing – original draft. **Yangyang Ren:** Methodology, Formal analysis. **Jianling Zhao:** Formal analysis. **Shuo Sun:** Formal analysis. **Xihua Du:** Formal analysis. **Mengmeng Wang:** Formal analysis. **Gang Ma:** Formal analysis. **Haoran Yu:** Formal analysis. **Lanlan Li:** Validation, Project administration. **Xiaofei Yu:** Validation, Project administration. **Xinghua Zhang:** Validation, Project administration. **Zunming Lu:** Validation, Project administration. **Xiaojing Yang:** Conceptualization, Formal analysis, Funding acquisition.

Declaration of Competing Interest

The authors declare that they have no known competing financial interests or personal relationships that could have appeared to influence the work reported in this paper.

Appendix A. Supporting information

Supplementary data associated with this article can be found in the online version at doi:10.1016/j.apcatb.2022.121494.

References

[1] M.P. Suh, H.J. Park, T.K. Prasad, D.W. Lim, Hydrogen storage in metal-organic frameworks, Chem. Rev. 112 (2012) 782–835.
[2] U. Eberle, M. Felderhoff, F. Schueth, Chemical and physical solutions for hydrogen storage, Angew. Chem. Int. Ed. 48 (2009) 6608–6630.
[3] H. Liu, X. Liu, W. Yang, M. Shen, S. Geng, C. Yu, B. Shen, Y. Yu, Photocatalytic dehydrogenation of formic acid promoted by a superior PdAg@g-C3N4 Mott-Schottky heterojunction, J. Mater. Chem. A 7 (2019) 2022–2026.
[4] Z.W. Tang, X.W. Chen, H. Chen, L.M. Wu, X.B. Yu, Metal-free catalysis of ammonia-borane dehydrogenation/regeneration for a highly efficient and facilely recyclable hydrogen-storage material, Angew. Chem. Int. Ed. 52 (2013) 5832–5835.

[5] W. Li, Y. Zhao, Y. Liu, M. Sun, G.I.N. Waterhouse, B. Huang, K. Zhang, T. Zhang, S. Lu, Exploiting Ru-induced lattice strain in CoRu nanoalloys for robust bifunctional hydrogen production, Angew. Chem. Int. Ed. 60 (2020) 3290–3298.

[6] T. Wang, X. Cao, L. Jiao, Ni2P/NiMoP heterostructure as a bifunctional electrocatalyst for energy-saving hydrogen production, eScience 1 (2021) 69–74.

[7] A. Staubitz, A.P.M. Robertson, I. Manners, Ammonia-borane and related compounds as dihydrogen sources, Chem. Rev. 110 (2010) 4079–4124.

[8] Z. Tang, H. Chen, X. Chen, L. Wu, X. Yu, Graphene oxide based recyclable dehydrogenation of ammonia borane within a hybrid nanostructure, J. Am. Chem. Soc. 134 (2012) 5464–5467.

[9] Q. Wang, F. Fu, S. Yang, M. Martinez Moro, M.D.L.A. Ramirez, S. Moya, L. Salmon, J. Ruiz, D. Astruc, Dramatic synergy in CoPt nanocatalysts stabilized by "click" dendrimers for evolution of hydrogen from hydrolysis of ammonia borane, ACS Catal. 9 (2018) 1110–1119.

[10] F. Fu, C. Wang, Q. Wang, A.M. Martinez-Villacorta, A. Escobar, H. Chong, X. Wang, S. Moya, L. Salmon, E. Fouquet, J. Ruiz, D. Astruc, Highly selective and sharp volcano-type synergistic Ni2Pt@ZIF-8-catalyzed hydrogen evolution from ammonia borane hydrolysis, J. Am. Chem. Soc. 140 (2018) 10034–10042.

[11] K. Yao, C. Zhao, N. Wang, T. Li, W. Lu, J. Wang, An aqueous synthesis of porous PtPd nanoparticles with reversed bimetallic structures for highly efficient hydrogen generation from ammonia borane hydrolysis, Nanoscale 12 (2020) 638–647.

[12] Q. Yao, Z.-H. Lu, W. Huang, X. Chen, J. Zhu, High Pt-like activity of the Ni–Mo/ graphene catalyst for hydrogen evolution from hydrolysis of ammonia borane, J. Mater. Chem. A 4 (2016) 8579–8583.

[13] S. Akbayrak, Z. Ozcifci, A. Tabak, Noble metal nanoparticles supported on activated carbon: Highly recyclable catalysts in hydrogen generation from the hydrolysis of ammonia borane, J. Colloid Interface Sci. 546 (2019) 324–332.

[14] Y. Liu, X. Yong, Z. Liu, Z. Chen, Z. Kang, S. Lu, Unified catalyst for efficient and stable hydrogen production by both the electrolysis of water and the hydrolysis of ammonia borane, Adv. Sustain. Syst. 3 (2019) 1800161.

[15] J. Li, Q. Guan, H. Wu, W. Liu, Y. Lin, Z. Sun, X. Ye, X. Zheng, H. Pan, J. Zhu, S. Chen, W. Zhang, S. Wei, J. Lu, Highly active and stable metal single-atom catalysts achieved by strong electronic metal-support interactions, J. Am. Chem. Soc. 141 (2019) 14515–14519.

[16] X. Yang, F. Cheng, Z. Tao, J. Chen, Hydrolytic dehydrogenation of ammonia borane catalyzed by carbon supported Co core–Pt shell nanoparticles, J. Power Sources 196 (2011) 2785–2789.

[17] W. Chen, D. Li, Z. Wang, G. Qian, Z. Sui, X. Duan, X. Zhou, I. Yeboah, D. Chen, Reaction mechanism and kinetics for hydrolytic dehydrogenation of ammonia borane on a Pt/CNT catalyst, AIChE J. 63 (2017) 60–65.

[18] W. Chen, W. Fu, G. Qian, B. Zhang, X.Duan Chen, X. Zhou, Synergistic Pt-WO3 dual active sites to boost hydrogen production from ammonia borane, iScience 23 (2020), 100922.

[19] J. Hu, Z. Chen, M. Li, X. Zhou, H. Lu, Amine-capped Co nanoparticles for highly efficient dehydrogenation of ammonia borane, ACS Appl. Mater. Interfaces 6 (2014) 13191–13200.

[20] Y. Yamada, K. Yano, Q. Xu, S. Fukuzumi, Cu/Co3O4 nanoparticles as catalysts for hydrogen evolution from ammonia borane by hydrolysis, J. Phys. Chem. C 114 (2010) 16456–16462.

[21] H. Zhang, Y. Fan, B. Liu, Y. Liu, S. Ashraf, X. Wu, G. Han, J. Gao, B. Li, Birdcage-type CoOx-carbon catalyst derived from metal-organic frameworks for enhanced hydrogen generation, ACS Sustain. Chem. Eng. 7 (2019) 9782–9792.

[22] Y. Yang, S.W. Niu, D.D. Han, T.Y. Liu, G.M. Wang, Y. Li, Progress in developing metal oxide nanomaterials for photoelectrochemical water splitting, Adv. Energy Mater. 7 (2017) 26.

[23] A. Singh, L. Spiccia, Water oxidation catalysts based on abundant 1st row transition metals, Coord. Chem. Rev. 257 (2013) 2607–2622.

[24] W. Wang, Z. Dai, R. Jiang, Q. Li, X. Zheng, W. Liu, Z. Luo, Z. Xu, J. Peng, Highly phosphatized magnetic catalyst with electron transfer induced by quaternary synergy for efficient dehydrogenation of ammonia borane, ACS Appl. Mater. Interfaces 12 (2020) 43854–43863.

[25] S. Zhang, M. Li, L. Li, F. Dushimimana, J. Zhao, S. Wang, J. Han, X. Zhu, X. Liu, Q. Ge, H. Wang, Visible-light-driven multichannel regulation of local electron density to accelerate activation of O–H and B–H bonds for ammonia borane hydrolysis, ACS Catal. 10 (2020) 14903–14915.

[26] P. Li, R. Chen, S. Zhao, W.Q. Li, Y.A. Lin, Y. Yu, Architecture control and electronic structure engineering over Ni-based nitride nanocomposite for boosting ammonia borane dehydrogenation, Appl. Catal. B 298 (2021), 120523.

[27] D. Ji, L. Fan, L. Tao, Y. Sun, M. Li, G. Yang, Q.T. Thang, S. Ramakrishna, S. Guo, The Kirkendall effect for engineering oxygen vacancy of hollow Co3O4 nanoparticles toward high-performance portable zinc-air batteries, Angew. Chem. Int. Ed. 58 (2019) 13840–13844.

[28] X. Wang, X. Li, J. Mu, S. Fan, X. Chen, L. Wang, Z. Yin, M. Tade, S. Liu, Oxygen vacancy-rich porous Co3O4 nanosheets toward boosted NO reduction by CO and CO oxidation: insights into the structure-activity relationship and performance enhancement mechanism, ACS Appl. Mater. Interfaces 11 (2019) 41988–41999.

[29] J. Ding, L. Li, H. Zheng, Y. Zuo, X. Wang, H. Li, S. Chen, D. Zhang, X. Xu, G. Li, Co3O4-CuCoO2 nanomesh: an interface-enhanced substrate that simultaneously promotes CO adsorption and O2 activation in H2 purification, ACS Appl. Mater. Interfaces 11 (2019) 6042–6053.

[30] S.B. Kalidindi, U. Sanyal, B.R. Jagirdar, Nanostructured Cu and Cu@Cu2O core shell catalysts for hydrogen generation from ammonia-borane, Phys. Chem. Chem. Phys. 10 (2008) 5870–5874.

[31] S. Mounika, V. Krishnaveni, M.E. Dmello, S.B. Kalidindi, Copper(II)-assisted ammonia borane dehydrogenation: an insight, Eur. J. Inorg. Chem. 2021 (2021) 4000–4006.

[32] G. Li, S. Liu, Y. Pan, T. Zhou, J. Ding, Y. Sun, Y. Wang, Self-templated formation of CuCo2O4 triple-shelled hollow microspheres for all-solid-state asymmetric supercapacitors, J. Alloy. Compd. 787 (2019) 694–699.

[33] Y. Zhang, L. Feng, W. Zhan, S. Li, Y. Li, X. Ren, P. Zhang, L. Sun, Co3O4 hollow porous nanospheres with oxygen vacancies for enhanced Li–O2 batteries, ACS Appl. Energy Mater. 3 (2020) 4014–4022.

[34] S. Kamari Kaverlavani, S.E. Moosavifard, A. Bakouei, Self-templated synthesis of uniform nanoporous CuCo2O4 double-shelled hollow microspheres for high-performance asymmetric supercapacitors, Chem. Commun. 53 (2017) 1052–1055.

[35] K.N. Patil, D. Prasad, J.T. Bhanushali, H. Kim, A.B. Atar, B.M. Nagaraja, A. H. Jadhav, Sustainable hydrogen eeneration by catalytic hydrolysis of NaBH4 using tailored nanostructured urchin-like CuCo2O4 spinel catalyst, Catal. Lett. 150 (2019) 586–604.

[36] C. Ma, C. Yang, B. Wang, C. Chen, F. Wang, X. Yao, M. Song, Effects of H2O on HCHO and CO oxidation at room-temperature catalyzed by MCo2O4 (M=Mn, Ce and Cu) materials, Appl. Catal. B 254 (2019) 76–85.

[37] K. Xiang, Z. Xu, T. Qu, Z. Tian, Y. Zhang, Y. Wang, M. Xie, X. Guo, W. Ding, X. Guo, Two dimensional oxygen-vacancy-rich Co3O4 nanosheets with excellent supercapacitor performances, Chem. Commun. 53 (2017) 12410–12413.

[38] X. Chen, S. Cai, E. Yu, J. Li, J. Chen, H. Jia, Photothermocatalytic performance of ACo2O4 type spinel with light-enhanced mobilizable active oxygen species for toluene oxidation, Appl. Surf. Sci. 484 (2019) 479–488.

[39] X. Dong, X. Duan, Z. Sun, X. Zhang, C. Li, S. Yang, B. Ren, S. Zheng, D.D. Dionysiou, Natural illite-based ultrafine cobalt oxide with abundant oxygen-vacancies for highly efficient Fenton-like catalysis, Appl. Catal. B 261 (2020) 118214.

[40] J. Zheng, X. Liu, L. Zhang, Design of porous double-shell Cu2O@CuCo2O4 Z-Scheme hollow microspheres with superior redox property for synergistic photocatalytic degradation of multi-pollutants, Chem. Eng. J. 389 (2020), 124339.

[41] J. Li, X. Ren, H. Lv, Y. Wang, Y. Li, B. Liu, Highly efficient hydrogen production from hydrolysis of ammonia borane over nanostructured Cu@CuCoOx supported on graphene oxide, J. Hazard. Mater. 391 (2020), 122199.

[42] G. Wei, J. He, W. Zhang, X. Zhao, S. Qiu, C. An, Rational design of Co(II) dominant and oxygen vacancy defective CuCo2O4@CQDs hollow spheres for enhanced overall water splitting and supercapacitor performance, Inorg. Chem. 57 (2018) 7380–7389.

[43] G. Li, C. Zhang, Z. Wang, H. Huang, H. Peng, X. Li, Fabrication of mesoporous Co3O4 oxides by acid treatment and their catalytic performances for toluene oxidation, Appl. Catal. A 550 (2018) 67–76.

[44] D. Yan, W. Wang, X. Luo, C. Chen, Y. Zeng, Z. Zhu, NiCo2O4 with oxygen vacancies as better performance electrode material for supercapacitor, Chem. Eng. J. 334 (2018) 864–872.

[45] K. Yao, N. Wang, Z. Li, W. Lu, J. Wang, Ionic liquid-modulated synthesis of porous worm-like gold with strong sers response and superior catalytic activities, Nanomaterials 9 (2019) 1772.

[46] W. Chen, W. Zheng, J. Cao, W. Fu, G. Qian, D. Chen, X. Zhou, X. Duan, Atomic insights into robust Pt–PdO interfacial site-boosted hydrogen generation, ACS Catal. 10 (2020) 11417–11429.

[47] W. Chen, D. Li, C. Peng, G. Qian, X. Duan, D. Chen, X. Zhou, Mechanistic and kinetic insights into the Pt-Ru synergy during hydrogen generation from ammonia borane over PtRu/CNT nanocatalysts, J. Catal. 356 (2017) 186–196.

[48] S. Rej, L. Mascaretti, E.Y. Santiago, O. Tomanec, Š. Kment, Z. Wang, R. Zbořil, P. Fornasiero, A.O. Govorov, A. Naldoni, Determining plasmonic hot electrons and photothermal effects during H2 evolution with TiN–Pt nanohybrids, ACS Catal. 10 (2020) 5261–5271.

[49] C. Cui, Y. Liu, S. Mehdi, H. Wen, B. Zhou, J. Li, B. Li, Enhancing effect of Fe-doping on the activity of nano Ni catalyst towards hydrogen evolution from NH3BH3, Appl. Catal., B 265 (2020), 118612.

[50] D. Liu, C. Zhang, Y. Yu, Y. Shi, Y. Yu, Z. Niu, B. Zhang, Hydrogen evolution activity enhancement by tuning the oxygen vacancies in self-supported mesoporous spinel oxide nanowire arrays, Nano Res. 11 (2017) 603–613.